PAPER

Efficient coupling of MnO$_2$/TiN on carbon cloth positive electrode and Fe$_2$O$_3$/TiN on carbon cloth negative electrode for flexible ultra-fast hybrid supercapacitors†

Mai Li, [ID] *[a] Kailan Zhu,[a] Zheyi Meng,*[b] Ruihua Hu,[a] Jiale Wang,[a] Chunrui Wang [ID] [a] and Paul K. Chu [ID] [b]

Recent research and development of energy storage devices has focused on new electrode materials because of the critical effects on the electrochemical properties of supercapacitors. In particular, MnO$_2$ and Fe$_2$O$_3$ have drawn extensive attention because of their low cost, high theoretical specific capacity, environmental friendliness, and natural abundance. In this study, MnO$_2$ ultrathin nanosheet arrays and Fe$_2$O$_3$ nanoparticles are fabricated on TiN nanowires to produce binder-free core–shell positive and negative electrodes for a flexible and ultra-fast hybrid supercapacitor. The MnO$_2$/TiN/CC electrode shows larger pseudocapacitance contributions than MnO$_2$/CC. For example, at a scanning rate of 2 mV s^{-1}, the pseudocapacitance contribution of MnO$_2$/TiN/CC is 87.81% which is nearly 25% bigger than that of MnO$_2$/CC (71.26%). The supercapacitor can withstand a high scanning rate of 5000 mV s^{-1} in the 2 V window and exhibits a maximum energy density of 71.19 W h kg^{-1} at a power density of 499.79 W kg^{-1}. Even at 5999.99 W kg^{-1}, it still shows an energy density of 31.3 W h kg^{-1} and after 10 000 cycles, the device retains 81.16% of the initial specific capacitance. The activation mechanism is explored and explained.

1. Introduction

Electrochemical supercapacitors have attracted much attention because of the rapid recharging ability, high power density, environment friendliness, and potential to bridge the gap between high-power devices and lithium-ion batteries.[1,2] Recent research has focused on new electrode materials and their critical influence on the electrochemical properties of supercapacitors. Among the various types of electrode materials, manganese oxide (MnO$_2$) is especially interesting because of the low cost, high theoretical specific capacity (1370 F g^{-1}), environmental benignity, and natural abundance boding well for rechargeable lithium-ion batteries and supercapacitors.[3–5] However, nanocrystalline MnO$_2$ suffers from low specific capacitance and rate capability because of the low electrical conductivity (10^{-5} to 10^{-6} S cm^{-1})[6] as well as severe aggregation and volume expansion during electrochemical reactions consequently limiting practical applications.[7]

One possible means to improve the electrical conductivity and specific area of MnO$_2$ is to produce nanostructured MnO$_2$ thin films on conductive carbon-based materials, nanowires, nanosheets, or conductive polymers, for example, MnO$_2$/nitrogen-doped carbon,[8] N + MnO$_2$@TiC/CC,[9] MnO$_2$/CuCo$_2$O$_4$,[10] and γ-MnO$_2$/PANI.[11] In this work, a novel composite structure composed of MnO$_2$ ultrathin nanosheet is prepared on the TiN nanowire array on a piece of conductive carbon cloth (MnO$_2$/TiN/CC) to form a binder-free and flexible positive electrode for supercapacitors as shown in Fig. 1 of the preparation process and structure of electrodes. The nanostructured array of TiN with a small diameter prepared on conductive carbon cloth (TiN/CC) has distinctive advantages such as short diffusion lengths of ions in the electrolyte, excellent substrate conductivity, large surface area, and loading of a large amount of active materials, consequently resulting in improved charging–discharging rates as well as energy and power densities.[12,13]

In order to complement the MnO$_2$ positive electrode in the asymmetrical hybrid supercapacitor, nanoscale Fe$_2$O$_3$ is deposited on TiN/CC to form the Fe$_2$O$_3$/TiN/CC as the negative electrode. Fe$_2$O$_3$ has advantages similar to MnO$_2$ such as natural abundance, multiple morphologies, crystallographic

[a]College of Science, Donghua University, Shanghai 201620, China. E-mail: limai@dhu.edu.cn

[b]State Key Laboratory for Modification of Chemical Fibers and Polymer Materials, College of Material Science, Donghua University, Shanghai 201620, China. E-mail: mengzheyi@dhu.edu.cn

[c]Department of Physics, Department of Materials Science and Engineering, Department of Biomedical Engineering, City University of Hong Kong, Tat Chee Avenue, Kowloon, Hong Kong, China
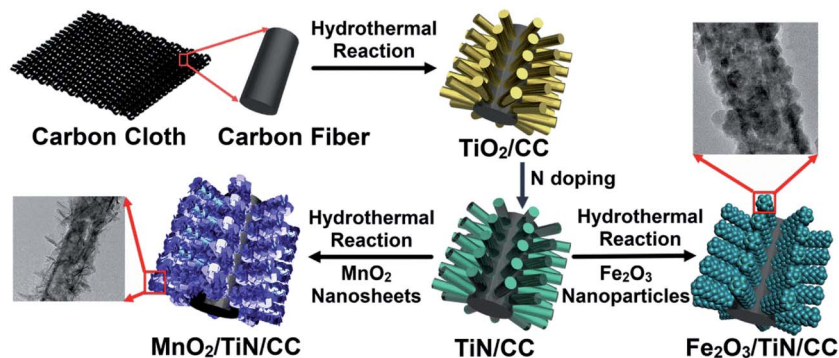
Fig. 1 Schematic illustration of the electrodes synthesis process.

modification, high thermal stability, and most importantly, high theoretical specific capacity of 3000 F g^{-1}.[14] Unfortunately, Fe$_2$O$_3$ also suffers from poor electrical conductivity leading to low capability and cycling stability. Herein, Fe$_2$O$_3$ nanoparticles are prepared on TiN nanowires to form a core–shell structure to solve the problems that plague Fe$_2$O$_3$ in the redox reaction. The asymmetrical hybrid supercapacitor comprising the MnO$_2$/TiN/CC positive electrode and Fe$_2$O$_3$/TiN/CC negative electrode is demonstrated to have excellent properties in 1 M Na$_2$SO$_4$ electrolyte and the enhancement mechanism is investigated.

2. Materials characterization and electrochemical evaluation

2.1 Materials characterization

The morphology, microstructure, elemental composition, and elemental distributions were characterized by scanning electron microscopy (SEM, JEOL JSM-7001F, Japan) and energy-dispersive X-ray spectroscopy (EDS). The crystal structure was examined by X-ray diffraction (XRD, Rigaku, RINT2000, Japan) and the elemental composition and chemical states were determined by X-ray photoelectron spectroscopy (XPS, Kratoms Axis Ultra DLD). Transmission electron micrographs (TEM) were taken on the JEOL (JEM-2000 FX) microscope at 200 kV.

2.2 Electrochemical measurements

The CHI660E electrochemical workstation was used in the electrochemical assessment. Using 1.0 M Na$_2$SO$_4$ as the electrolyte, CC, MnO$_2$/CC, TiN/CC, MnO$_2$/TiN/CC, or Fe$_2$O$_3$/TiN/CC was the working electrode, whereas the saturated calomel electrode and platinum wire were the reference electrode and counter electrodes, respectively. Galvanostatic charging–discharging (GCD), cyclic voltammetry (CV), and electrochemical impedance spectroscopy (EIS) were carried out to determine the electrochemical properties of the electrodes.

The specific capacitance of the electrode C_s is determined by eqn (1) and the energy (E) and power (P) densities are determined by eqn (2) and (3):[15]

$$C_s = \frac{I \times \Delta t}{m \times \Delta V} \tag{1}$$

$$E = \frac{C \times (\Delta V)^2}{2 \times 3.6} \tag{2}$$

$$P = \frac{E \times 3600}{\Delta t}, \tag{3}$$

where C_s (F g^{-1}) is the specific capacitance, I (A) is the current density during charging and discharging, Δt (s) is the discharging time, m (g) is the mass of the active substance in the electrode, ΔV (V) is the pressure drop in the test, v (V s^{-1}) is the scanning rate in CV, and $\int i dV$ is the area of the CV curve.

3. Experimental details

3.1 Materials synthesis

Analytical grade chemicals were used without further purification. A piece of carbon cloth (20 × 20 cm^2 size) was cleaned by a nitrogen plasma using a power of 200 W for 10 minutes under vacuum. Subsequently, 0.45 ml of titanium butoxide and 15 titanium butoxide were added to 15 ml of deionized water. The solution was placed in a 50 ml Teflon steel autoclave together with a piece of clean carbon cloth (2 × 2 cm^2). After the reaction at 150 °C for 24 h, the product was kept warm for 1 h at 450 °C to form TiO$_2$/CC.[16] The TiN NTAs were prepared by annealing the TiO$_2$ nanotube arrays in ammonia to form the TiN/CC.[17] The prepared TiN/CC was cut into 0.5 cm^2 and weighed for the following experiments.

The MnO$_2$ nanosheets were fabricated on TiN/CC hydrothermally. 1 mmol KMnO$_4$ and 1.2 mmol H$_2$SO$_4$ were dissolved in 20 ml of deionized water and stirred for 30 min. The solution containing TiN/CC were transferred to a Teflon-sealed stainless-steel autoclave and heated to 180 °C for 8 h. After cooling to room temperature, the sample was taken out, washed with deionized water, and dried at 60 °C for 10 h. MnO$_2$/CC was also prepared by a similar method as MnO$_2$/TiN/CC, except that TiN/CC was replaced by CC with the area of 0.5 cm^2.

Fe$_2$O$_3$ was also fabricated on TiN/CC to form the negative electrode. 1 mmol ferric nitrate was added to 15 mmol urea and the solution put in a reactor with the TiN/CC placed in front. The hydrothermal reaction proceeded for 8 hours at 120 °C followed by natural cooling. The Fe$_2$O$_3$/TiN/CC electrode was

formed by rinsing with deionized water and ethanol and dried at 60 °C for 10 h.

3.2 Fabrication of the asymmetrical hybrid supercapacitor

The asymmetrical hybrid supercapacitor was assembled with the MnO₂/TiN/CC and Fe₂O₃/TiN/CC electrodes separated by a polyethylene (PE) membrane. The PE membrane was pre-treated and dipped in NaSO₄ for 10 min and assembled with the electrodes in a CR2032 battery case in 1 M NaSO₄ electrolyte. Galvanostatic charging–discharging (GCD), cyclic voltammetry (CV), and electrochemical impedance spectroscopy (EIS) were carried out to determine the electrochemical properties of the electrodes.

4. Results and discussion

Fig. 2(a)–(d) and S1† depict the SEM images of TiN/CC and MnO₂/TiN/CC at different magnifications. The TiN nanowires with an average diameter of 100 nm are distributed uniformly and densely on the carbon cloth forming a cross-linked porous conductive framework boding well for rapid electron and ion transfer. Fig. 2(c) and (d) show the SEM images of MnO₂/TiN/CC at different magnifications. The MnO₂ nanosheets and TiN nanowires form core–shells with a diameter of about 300 nm that adhere firmly to the carbon cloth. This special structure is expected to expedite adsorption, desorption, and migration of ions in the electrochemical redox process. The TEM images of the MnO₂/TiN core–shell structure at different magnifications are displayed in Fig. 2(e) and (f). The lattice spacings of 0.24 nm, 0.21 nm, and 0.23 nm correspond to the (211) plane of MnO₂, (200) plane of TiN, and (111) plane of TiN, respectively. The SAED pattern (inset in Fig. 2(e)) shows that the radii of the three diffraction rings are 0.24, 0.22, and 0.14 nm, corresponding to the (101), (200) and (300) planes of MnO₂, respectively, and MnO₂ is not a single crystal. A regular lattice structure around the diffraction ring of MnO₂ can also be observed indicating the SAED pattern of TiN.[15] The core–shell composed of MnO₂ nanosheets and TiN nanotubes is confirmed by the elemental maps of MnO₂/TiN in Fig. 2(g1) and (g2) and the elemental distributions are presented in Fig. 2(g3)–(g6). Nitrogen as a dopant is found uniformly on TiN and MnO₂ with a petal structure and evenly deposited on the surface of the TiN nanowires.
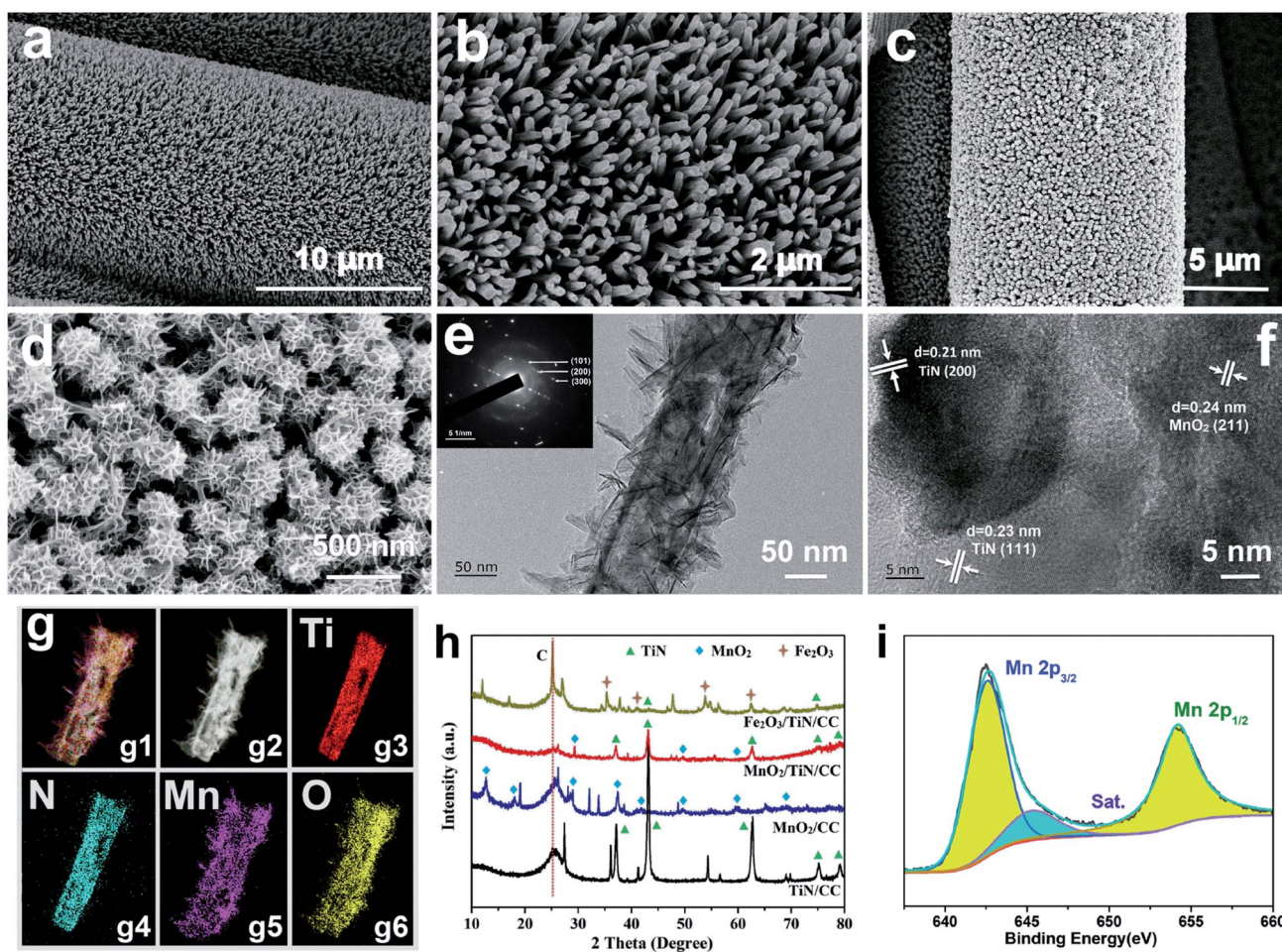

Fig. 2 SEM images: (a and b) TiN/CC and (c and d) MnO₂/TiN/CC; (e) TEM image and SAED pattern; (f) HR-TEM image and (g) EDS elemental maps of the MnO₂/TiN core–shell structure; (h) XRD patterns of TiN/CC, MnO₂/CC, MnO₂/TiN/CC, and Fe₂O₃/TiN/CC; (i) XPS Mn 2p spectrum of MnO₂@TiN/CC.

Fig. 2(h) shows the XRD diffraction patterns of TiN/CC, MnO$_2$/CC, MnO$_2$/TiN/CC, and Fe$_2$O$_3$/TiN/CC. The C peak at 25.74° and TiN peaks at 36.66°, 42.59°, 61.81°, 74.07°, and 77.96° can be indexed to PDF#38-1420 corroborating the TiN/CC structure. The peaks at 28.84°, 49.86°, and 60.27° stem from α-MnO$_2$ in MnO$_2$/CC and MnO$_2$/TiN/CC according to PDF#44-0141. The XRD patterns of Fe$_2$O$_3$ prepared on the carbon cloth with and without TiN are displayed as yellow lines in Fig. 2(h). Both samples exhibit peaks of Fe$_2$O$_3$ at 35.61°, 40.85°, 54.09°, and 62.45° corresponding to the (110), (113), (116) and (214) planes of α-Fe$_2$O$_3$ (PDF#33-0664), respectively.[18] The peak of TiN is not particularly obvious because MnO$_2$ or Fe$_2$O$_3$ covers the surface of the materials. Fig. 2(i) shows the XPS Mn 2p spectrum of MnO$_2$/TiN/CC revealing peaks at 642.5 eV and 654.2 eV which represent Mn 2p$_{3/2}$ and Mn 2p$_{1/2}$ of MnO$_2$, respectively. The satellite peak (sat) is related to α-MnO$_2$ consistent with previous results further confirming formation of MnO$_2$. Fig. S3(a)† shows the XPS Fe 2p spectrum of Fe$_2$O$_3$/TiN/CC. There are two Fe 2p peaks at 710.86 eV and 724.58 eV related to Fe 2p$_{3/2}$ and Fe 2p$_{1/2}$ in α-Fe$_2$O$_3$.[19]

As shown in Fig. 3(a) and (b), the electrochemical properties of MnO$_2$/CC and TiN/CC are similar, whereas MnO$_2$/TiN/CC shows the largest CV area and longest discharging time compared to MnO$_2$/CC and TiN/CC. According to the mass difference of substances before and after the deposition of MnO$_2$ as the active material, it can be calculated that the MnO$_2$ loading of MnO$_2$/CC is 0.58 mg cm^{-2} and the MnO$_2$/TiN/CC is 0.76 mg cm^{-2}. The discharging time of MnO$_2$/TiN/CC at a current density of 2 mA cm^{-2} is 120.2 s, but TiN/CC and MnO$_2$/CC show discharging time of only 35 s and 34.8 s, respectively. According to GCD results in Fig. 3(b), the total MnO$_2$ loading and eqn (1), the specific capacity of MnO$_2$/TiN/CC at 2 mA cm^{-2} is 318.41 F g^{-1}, which is 2.7 times bigger than that of MnO$_2$/CC (120.5 F g^{-1}). Hence, the multi-component core–shell structure plays an important role in the properties of the MnO$_2$-based electrode. Fig. 3(c) shows the CV curves of MnO$_2$/TiN/CC from 5 mV s^{-1} to 200 mV s^{-1}. The CV curves exhibit a rectangular shape and there is an obvious redox peak suggesting that the specific capacitance is mainly due to the Faraday pseudo capacitance. As the scanning rate goes up, the
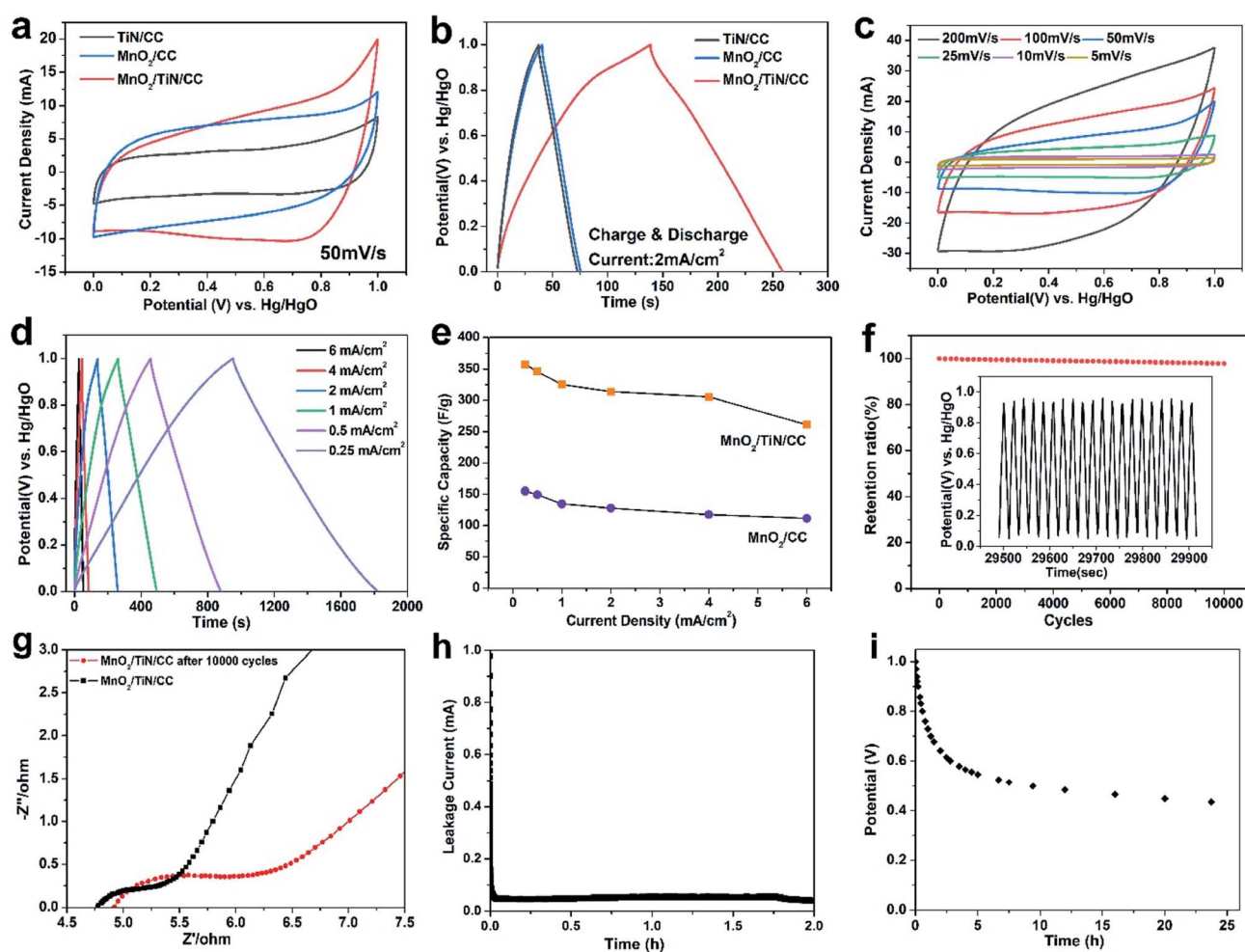

Fig. 3 (a) CV curves and (b) GCD plots of TiN/CC, MnO$_2$/CC, and MnO$_2$/TiN/CC; electrochemical properties of MnO$_2$/TiN/C: (c) CV curves acquired at different scanning rates, (d) GCD curves acquired at different current densities, (e) first cycle specific capacitances at different current densities, (f) 10 000 cycle charge–discharge performance test (inset showing the charge–discharge curve in the intermediate stage), (g) Nyquist plots of MnO$_2$/TiN/CC before and after 10 000 cycles, (h) leakage current and (i) self-discharge performance of MnO$_2$/TiN/CC.

redox peak gradually shifts to the middle indicating fast ion embedding rates. Hence, MnO_2/TiN/CC not only increases the loading amount of MnO_2, but also improves the contact area between MnO_2 and the electrolyte.

The GCD curves of MnO_2@TiN/CC acquired at current densities from 0.25 mA cm^{-2} to 6.0 mA cm^{-2} are displayed in Fig. 3(d) and (e) shows the corresponding specific capacitances of MnO_2@TiN/CC and MnO_2/CC. The GCD curves show a similar shape resembling an isosceles triangle with good symmetry, which indicates that the electrode has good reversibility and high coulomb efficiency. According to Fig. 3(d) and S2†(b), the loading mass of MnO_2 and eqn (S1),† the specific capacitances of MnO_2/TiN/CC are 365.37 F g^{-1}, 352.83 F g^{-1}, 330.64 F g^{-1}, 318.41 F g^{-1}, 309.87 F g^{-1}, and 261.83 F g^{-1} at current densities of 0.25 mA cm^{-2}, 0.5 mA cm^{-2}, 1 mA cm^{-2}, 2 mA cm^{-2}, 4 mA cm^{-2}, and 6 mA cm^{-2}, respectively. In comparison, MnO_2/CC shows capacitances of 155.66 F g^{-1}, 147.82 F g^{-1}, 127.87 F g^{-1}, 118.34 F g^{-1}, 104.22 F g^{-1}, and 95.82 F g^{-1} at current densities of 0.25 mA cm^{-2}, 0.5 mA cm^{-2}, 1 mA cm^{-2}, 2 mA cm^{-2}, 4 mA cm^{-2}, and 6 mA cm^{-2}, respectively. In order to analyze the change of specific capacity with current

density more clearly, the specific capacity of the above two electrodes are drawn in Fig. 3(e). Fig. 3(f) shows the stability of the MnO_2@TiN/CC electrode after 10 000 cycles. The specific capacitances of MnO_2@TiN/CC at a current density of 3 mA cm^{-2} before cycling is 310.7 F g^{-1} and after 10 000 cycles, it increases by only 2.1% to 304.2 F g^{-1}. The impedance data of the MnO_2@TiN/CC before and after 10 000 cycles are presented in Fig. 3(g). The Nyquist curves exhibit an arc in the high frequency region and an oblique line in the low frequency regime. In the high frequency region, the intersection points between the semicircle and Z' axis changes from 4.75 Ω to 4.92 Ω, indicating that MnO_2 dissolves continuously and the solution impedance increases with cycling. The diameter of the semicircle in the Nyquist plots increases with cycling as well. Before cycling, the end of the semicircle is about 5.3 Ω and after 10 000 cycles, it changes to 6.4 Ω. Furthermore, with increasing GCD cycles, the slope of low frequency region decreases, implying that the electrochemical performance worsens gradually.

For practical applications, it is important to evaluate the leakage current and self-discharge performance to analyze the
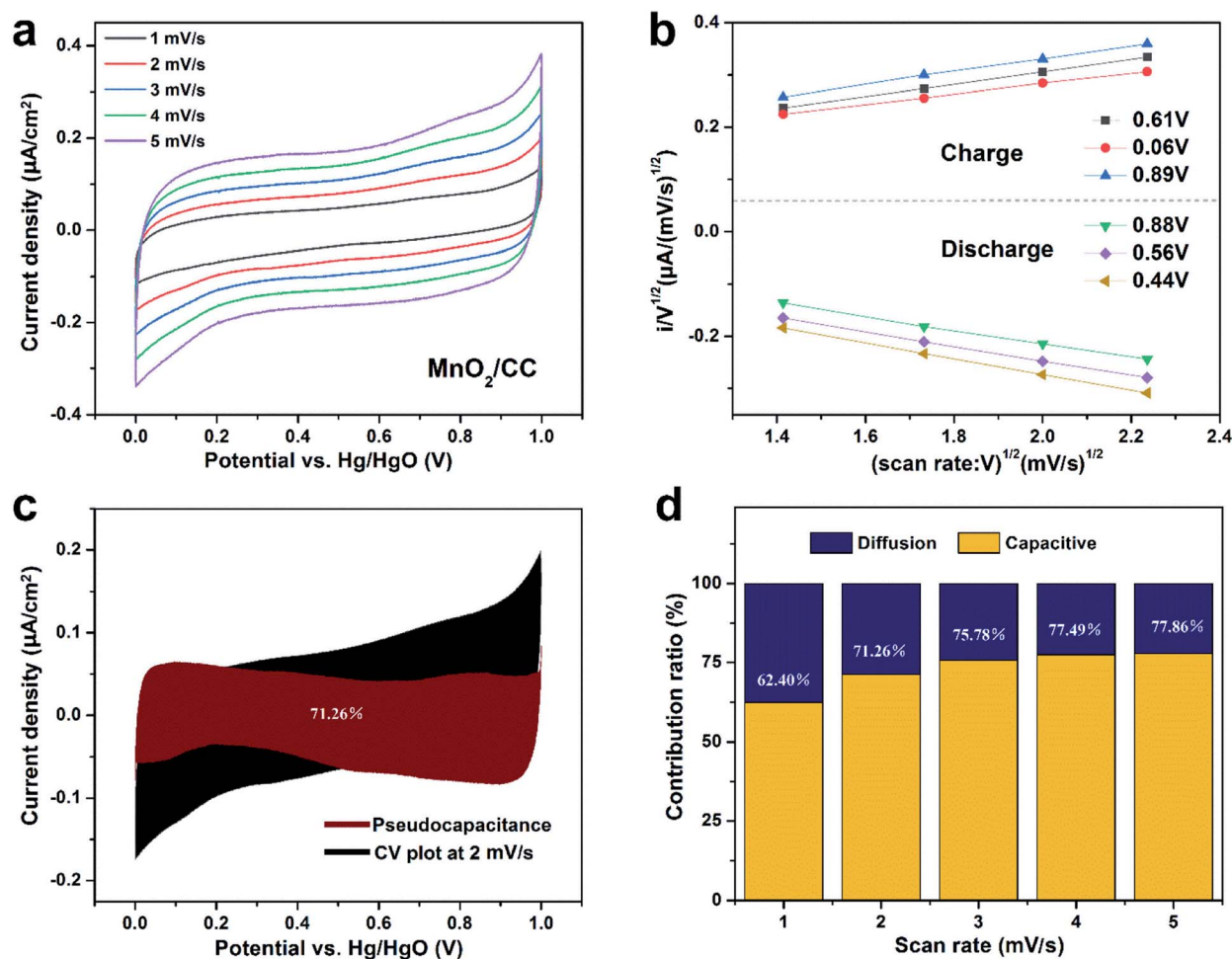

Fig. 4 (a) CV curves of MnO_2/CC, (b) 6 selected sets of CV data at various voltages for the calculation of k_1 using eqn (4), (c) pseudocapacitance of MnO_2/CC 2 mV s^{-1}, (d) ratio of pseudocapacitance contributions.

properties of the fabricated pseudocapacitive electrode.[20] In order to obtain the leakage current of the electrode, the MnO$_2$/TiN/CC is charged to 1 V under the current of 2 mA, and then a current flowing as the leakage current is applied to the electrode to keep the electrode potential at 1 V. Fig. 3(h) shows the curve of leakage current, which indicate that the leakage current drops to 0.048 mA in a short time and remains stable in the next two hours. The leakage current of our electrode is smaller than the a-NENCs electrode in 0.5 M K$_2$SO$_4$ electrolyte (0.08 mA),[21] Ni–Mn LDH/MnO$_2$ in 0.5 M Na$_2$SO$_4$ electrolyte (0.34 mA, after the unit conversion)[22] and 3D-NCS-3//N-rGO device (0.086 mA).[23] The low leakage current value of the MnO$_2$/TiN/CC suggests fewer reaction of byproduct impurities on the electrode and insignificant diffusion of electrolyte ions on the electrode surface due to the concentration gradient.[20] The potentials of the MnO$_2$/TiN/CC were then further measured for 25 h, and the time courses of the open circuit potential are shown in Fig. 3(i), which corresponds to the self-discharge process.[24] Based on the plots, the potential of electrode reduces gradually with the extending of time due to the leakage current, and they decrease quickly before 2 h and become gentle

subsequently after the following several hours. The plot shows a steady output potential of 641 mV after 5 h and still exhibits a good typical self-discharge rate, with about 436 mV retention after 25 h, which is comparable to previously reported values.[24]

To elucidate the mechanism of the MnO$_2$/CC and MnO$_2$/TiN/CC electrodes, the pseudocapacitance is calculated from the CV plots in Fig. 4(a) and 5(a) and by calculating k_1 (Fig. 4(b) and 5(b))[25] using eqn (4):

$$i(V)/v^{1/2} = k_1 v^{1/2} + k_2, \qquad (4)$$

where $i(V)$ is the CV current at the selected voltage (V), v is the scanning rate. k_1 is equal to the slope of each curve in Fig. 4(b) and 5(b) and the current for the pseudocapacitance at different voltage s is determined by $k_1 v$. Taking $k_1 v$ as the ordinate and corresponding voltage as the abscissa, the pseudocapacitance (red area) is obtained as shown in Fig. 4(c) and 5(c) and the relative pseudocapacitance contributions at different scanning rates are summarized in Fig. 4(d) and 5(d). The proportion of pseudocapacitance of MnO$_2$/CC calculated from the CV data at a scanning rate of 1 mV s^{-1} is about 62.40% but at 5 mV s^{-1}, the contribution is 77.86%. Hence, the MnO$_2$/CC electrode has
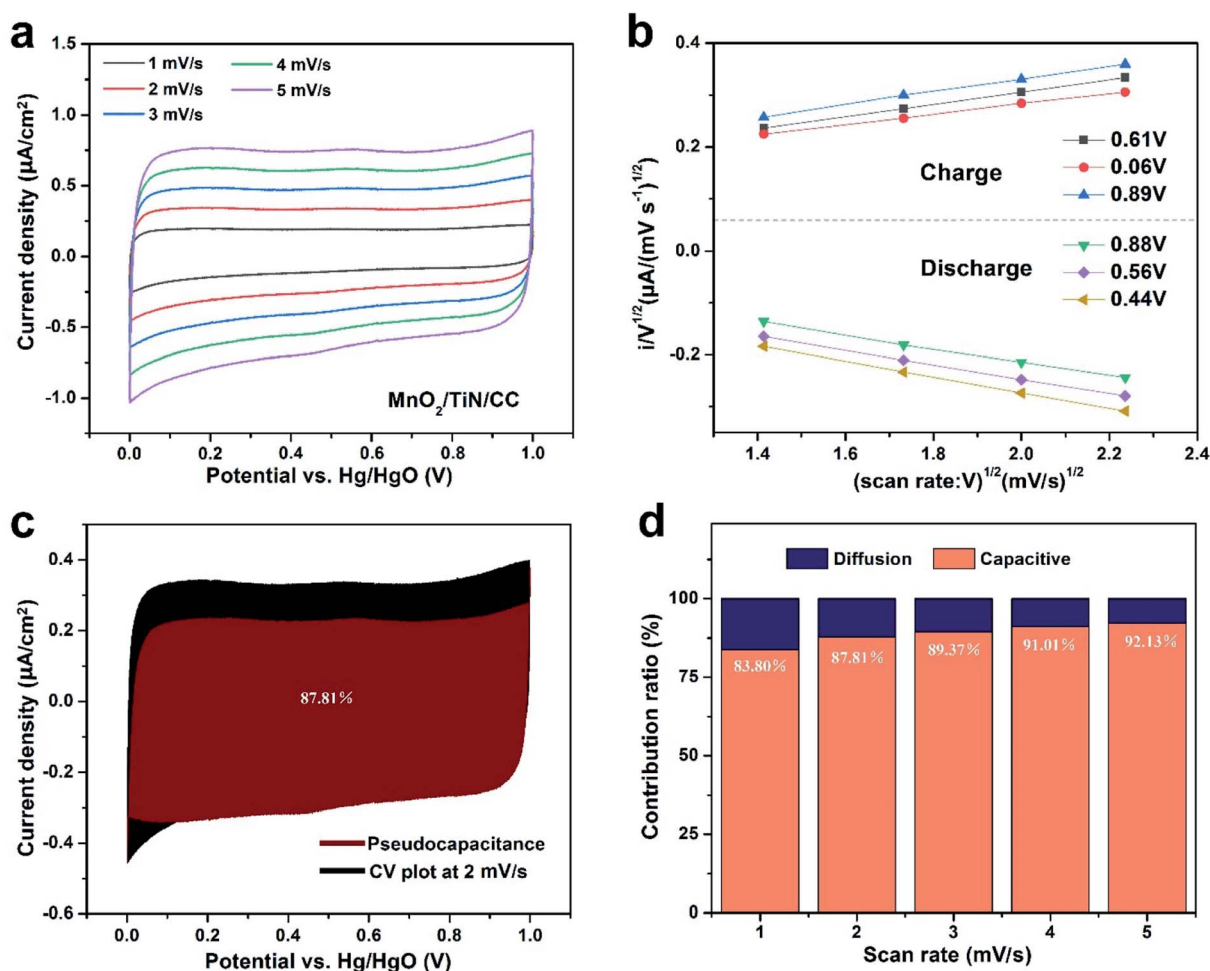

Fig. 5 (a) CV curves of MnO$_2$/TiN/CC, (b) 6 selected sets of CV data at various voltages for the calculation of k_1 using eqn (4), (c) pseudocapacitance of MnO$_2$/TiN/CC 2 mV s^{-1}, (d) ratio of pseudocapacitance contributions.
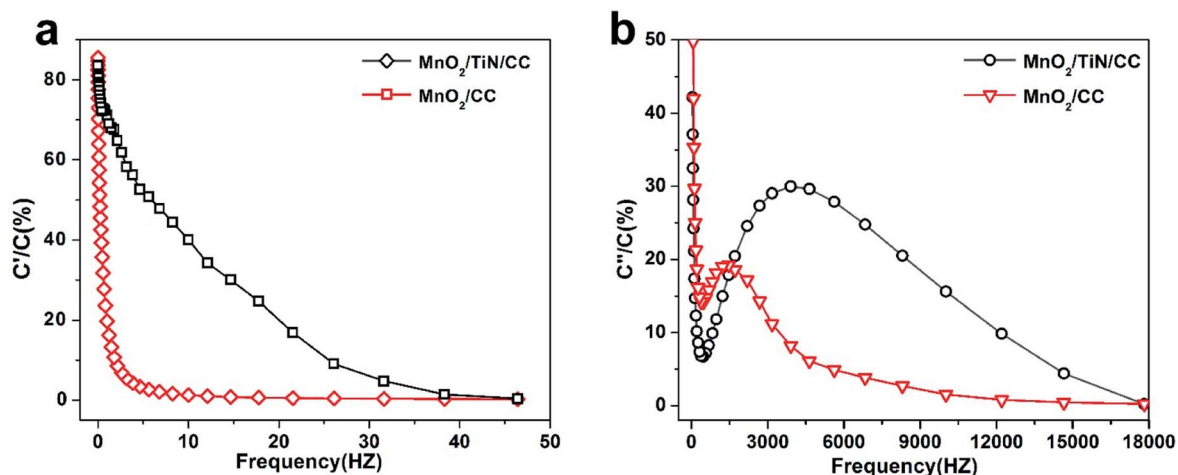
Fig. 6 (a) Plots of (a) real capacitance (C') and (b) imaginary capacitance (C') *vs.* frequency for the MnO_2/CC and $MnO_2/TiN/CC$ electrodes.

good pseudocapacitance characteristics. The pseudocapacitance of $MnO_2/TiN/CC$ can be derived from Fig. 5(c). The proportion of pseudocapacitance contribution of $MnO_2/TiN/CC$ electrode at each scanning rate from 1 mV s^{-1} to 5 mV s^{-1} is summarized in Fig. 5(d). The $MnO_2/TiN/CC$ electrode shows larger pseudocapacitance contributions than the MnO_2/CC. For example, at a scanning rate of 2 mV s^{-1}, the pseudocapacitance contribution of $MnO_2/TiN/CC$ is 87.81% which is nearly 25% bigger than that of MnO_2/CC (71.26%).

The relationship between impedance data and frequency of complex capacitance model is essential to analyze the supercapacitor electrodes. Real capacitance (C') and complex capacitance (C'') can be expressed by real, imaginary and total impedance with eqn (5)–(8), respectively[26,27]

$$Z(\omega) = \frac{1}{j\omega C(\omega)} \quad \text{in ohms} \tag{5}$$

$$C(\omega) = C'(\omega) - jC''(\omega) \text{ in farads} \tag{6}$$

Manipulation of eqn (3) and (4) leads to

$$C'(\omega) = \frac{-Z''(\omega)}{\omega |Z(\omega)|^2} \tag{7}$$

$$C''(\omega) = \frac{Z'(\omega)}{\omega |Z(\omega)|^2} \tag{8}$$

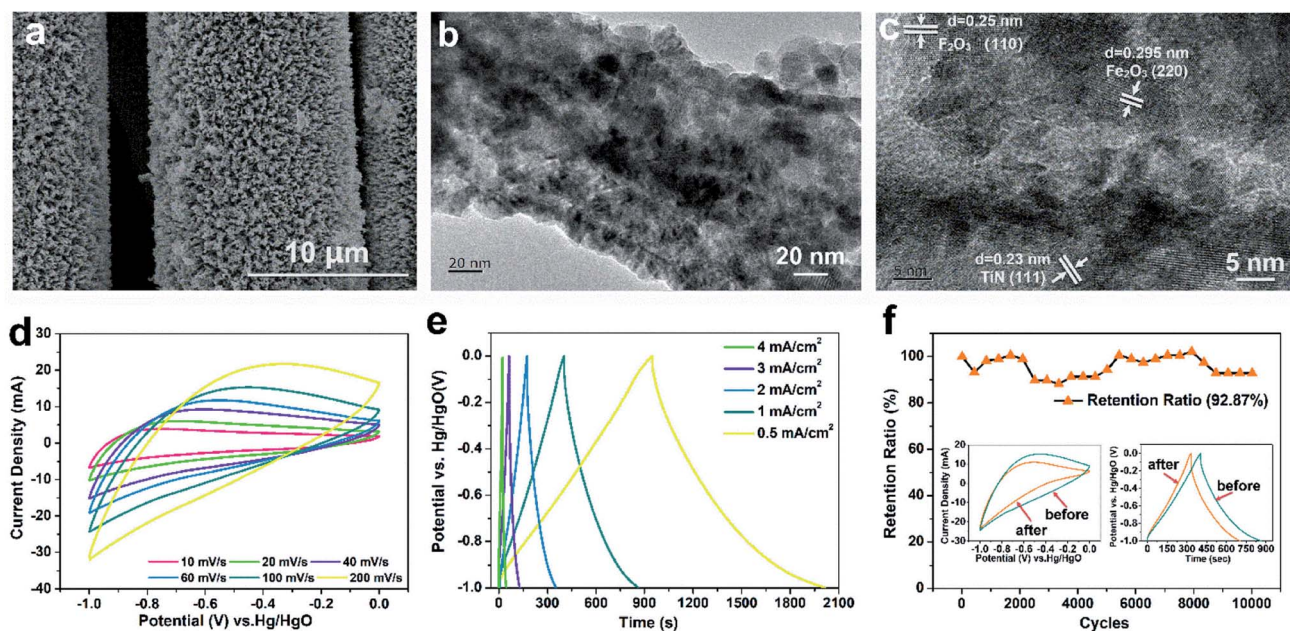where both C' and C'' have units of farads F.

Fig. 7 (a) SEM image of $Fe_2O_3/TiN/CC$; (b) TEM image and (c) HR-TEM image of the Fe_2O_3/TiN core−shell structure; electrochemical properties of $Fe_2O_3/TiN/CC$: (d) CV curves acquired at different scanning rates, (e) GCD curves acquired at different current densities, and (f) 10 000 cycle charge−discharge performance test .

C' describes the real part of the capacitance and shows the function of frequency can be displayed by the change available of stored energy. C'' describes the imaginary part of the capacitance and describes the energy loss corresponding to the form of energy dissipation.[27] For comparison between MnO$_2$/CC and MnO$_2$/TiN/CC electrodes, the real capacitance value C' and virtual capacitance value C'' are normalized against C_0 as the highest C values among the electrode.[27] Fig. 6(a) shows the relationship between the real part of the capacitance (C') and frequency. In comparison, the performance of MnO$_2$/TiN/CC is more like an ideal capacitor. When the frequency is greater than 50 Hz, the capacitance decreases and the sample shows pure resistance. Fig. 6(b) shows the relationship between the imaginary part C'' of capacitance and frequency, and the relaxation time constant τ as the quantitative measurement of the discharge speed of the device, which can be obtained from the C'' vs. frequency diagram. The relaxation time constant defines predominantly resistive behavior at frequencies above $1/\tau$ and capacitive behavior at frequencies below $1/\tau$. In other words, a smaller τ defines a higher percentage of useful capacitive

energy.[27,28] Fig. 6(b) shows that compare with MnO$_2$/CC, MnO$_2$/TiN/CC has a smaller τ, which indicate that the MnO$_2$/TiN/CC electrode has a fairly fast discharge time and potential to deliver stored energy with high power.[27]

Fig. 7(a) and S3(b)–(d)† depict the SEM images of the Fe$_2$O$_3$/TiN/CC negative electrode at different magnifications. Fe$_2$O$_3$ is uniformly deposited on the TiN nanowires forming a core–shell structure. Owing to the complex surface on TiN, Fe$_2$O$_3$ has a nanogranular structure and the diameter is about 10 nm. The TEM images of the Fe$_2$O$_3$/TiN core–shell at different magnifications are displayed in Fig. 7(b) and (c). As shown in Fig. 7(b), the Fe$_2$O$_3$ nanoparticles and TiN nanowires are combined and Fig. 7(c) shows spacings of 0.25 nm, 0.295 nm and 0.23 nm corresponding to the (110) plane of Fe$_2$O$_3$, (220) plane of Fe$_2$O$_3$, and (111) plane of TiN, respectively, thus confirming the Fe$_2$O$_3$/TiN core–shell structure.

Fig. 7(d) shows the CV curves of Fe$_2$O$_3$/TiN/CC at scanning rates from 10 mV s^{-1} to 200 mV s^{-1}. As the scanning rate goes up, the redox peak shifts gradually to the right, but the shape of the CV curves remains basically the same without obvious
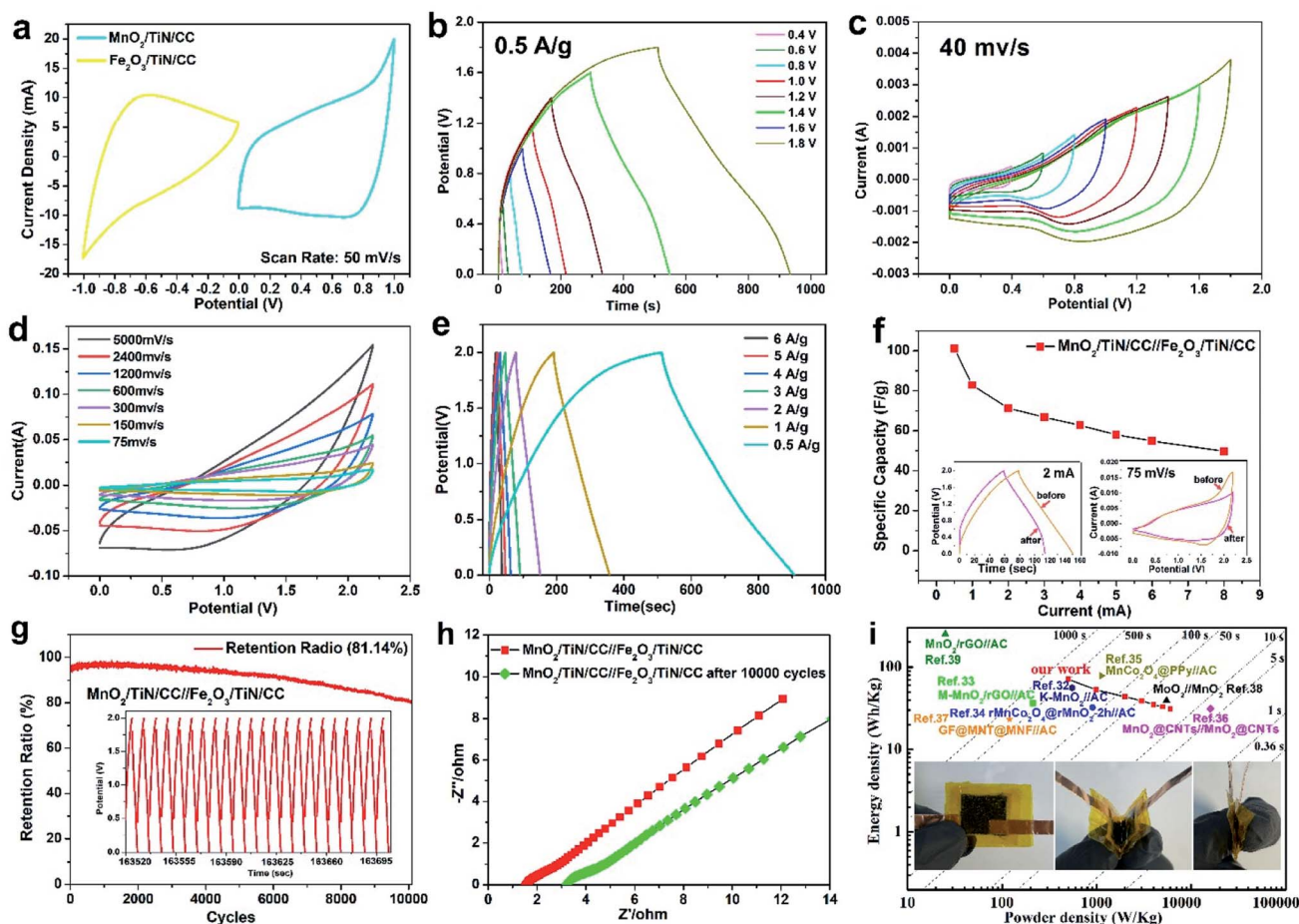

Fig. 8   (a) CV plots of MnO$_2$/TiN/CC and Fe$_2$O$_3$/TiN/CC at 50 mV s; electrochemical properties of MnO$_2$/TiN/CC//Fe$_2$O$_3$/TiN/CC: (b) GCD curves and (c) CV curves with different upper cut-off voltages, (d) GCD curves for different current densities, (e) CV curves acquired at different scanning rates, (f) specific capacitances at different current densities (insets showing the CV and GCD curves before and after 10 000 cycles in the GCD test), (g) 10 000 cycles GCD test (inset showing the long-term test), (h) Nyquist plots of the AHS before and after 10 000 cycles, and (i) Ragone plot showing the energy and power densities of the related materials and photographs of the device showing mechanical bending.

distortion, suggesting that the rates of insertion and extraction on the Fe_2O_3 surface are fast. As shown in the GCD curves (Fig. 7(e)) of $Fe_2O_3/TiN/CC$ from 0.5 mA cm^{-2} to 4 mA cm^{-2}, the shape of the curves resembles an isosceles triangle with good symmetry, implying that $Fe_2O_3/TiN/CC$ has good reversibility and high coulombic efficiency (98% at 0.5 mA cm^{-2}) in the charging and discharging process. For comparison, the CV curves and GCD curves of TiN/CC are presented in Fig. S4 and S5.† Without Fe_2O_3, the CV curves of TiN/CC are rectangular and the GCD curves resemble an isosceles triangle with good symmetry. The results indicate that the capacity of the TiN/CC electrode arises from ion adsorption and desorption on the TiN surface. At a current density of 0.5 mA cm^{-2}, the discharging time of $Fe_2O_3/TiN/CC$ is 958 s compared to 260.1 s for TiN/CC. Therefore, the $Fe_2O_3/TiN/CC$ core–shell structure plays an important role as the negative electrode in improving the characteristics. Fig. 7(f) shows the cycling performance of $Fe_2O_3/TiN/CC$ after 10 000 times at a current density of 8 mA cm^{-2}. In spite of capacity decay near the 2000th cycle, the capacity recovers after 3000 cycles. It is because of dissolution of Fe_2O_3 in the first two thousand cycles but after 3000 cycles, Fe_2O_3 is activated gradually. The inset in Fig. 7(f) reveals no significant change in the shape of the CV and GCD curves. Although the area of the CV curves decreases and the GCD discharging time also declines, the total capacity retention rate is quite high at 92.87%.

To demonstrate the practicality of the $MnO_2/TiN/CC$ and $Fe_2O_3/TiN/CC$ electrodes, an asymmetrical hybrid supercapacitor is assembled with $MnO_2/TiN/CC$ as the positive and $Fe_2O_3/TiN/CC$ as the negative electrode together with a PE membrane as the separator in the 1 M Na_2SO_4 electrolyte. All the supercapacitor device components are enclosed in a CR2025 battery cell.[29,30] Fig. 8(a) shows the CV curves of $MnO_2/TiN/CC$ and $Fe_2O_3/TiN/CC$ at 50 mV s^{-1}. The CV curves of $MnO_2/TiN/CC$ are at positive potentials from 0 to 1 V and $Fe_2O_3/TiN/CC$ has a negative potential from −1 to 0 V. The two CV curves show similar axial symmetry pertaining to the area, shape, and potential range, thereby indicating high adaptability and the EDLC behavior for both electrodes. Fig. 8(b) and (c) present the GCD and CV curves of $MnO_2/TiN/CC//Fe_2O_3/TiN/CC$ at different potential window. These curves do not exhibit obvious deformation in the 0–1.8 V window and the device can adapt to a working voltage up to 1.8 V. Furthermore, the device can withstand a high scanning rate of 5000 mV s^{-1} without showing distortion (Fig. 8(d)), corroborating to the large comparative area and rapid ion diffusion capability of the composite nanostructures on the MnO_2/TiN resulting in the fast charging–discharging properties of the device.[31] The charging–discharging curves at different current densities (Fig. 8(e)) show a triangular shape and so the device has good pseudocapacitive characteristics, fast I–V response, and excellent electrochemical reversibility. The relationship between the specific capacitance and current density in the GCD tests is shown in Fig. 8(f). The specific capacitance of the device is 102.8 F g^{-1} at a current density of 5 A g^{-1}, which is better than those of MnO_2-based devices reported in the literature, for instance, K–MnO_2//AC (83 F g^{-1} at 3 A g^{-1}),[32] M–MnO_2/rGO//AC (90.7 F g^{-1} at 0.25 A g^{-1}),[33] MnO_2@CNTs//MnO_2@CNTs (highest specific capacitance of 56 F g^{-1}[34] and GF@MNT@MNF//AC (51.50 F g^{-1} at 0.13 A g^{-1}).[29] More information can be found from Table 1.

Fig. 8(g) discloses that the supercapacitor device has excellent cycling ability up to 10 000 cycles at a high GCD current of 10 mA, and it should be emphasized such outstanding characteristics have rarely been observed from hybrid devices composed of MnO_2 and Fe_2O_3. Owing to the activation process, the cycling capacity is fully activated and improves significantly in the first 1000 cycles. After 10 000 cycles, the device retains 81.16% of the initial specific capacitance and fares better than most other devices as shown in Table 1. The inset in Fig. 8(g) shows the data for 20 cycles around the 8000th cycle in the 10 000-cycle test and demonstrates robust stability. To explain the attenuation before and after the 10 000th GCD cycle, EIS is conducted and the results are presented in Fig. 8(h). The intersection in the Nyquist curve and ordinate axis show that

Table 1 Comparison of the electrochemical properties of MnO_2-based hybrid supercapacitors

Electrode composition	Electrolyte	Potential window (V)	Specific capacity (F g^{-1})	Energy density (W h kg^{-1})	Power density (W kg^{-1})	Cycling retention (%)	Ref.
K–MnO_2//AC	1 M Na_2SO_4	2.2	83	56	550	98% (10 000-cycles)	32
M–MnO_2/rGO//AC	1 M Na_2SO_4	~1.6	90.7	36.4	212.5	88.2% (10 000-cycles)	33
r$MnCo_2O_4$@rMnO_2-2 h//AC	3 M KOH	1.6	91.2	32.4	904.9	81.8% (5000-cycles)	34
$MnCo_2O_4$@PPy//AC	2 M KOH	1.6	—	78.5	1121	95.5% (5000-cycles)	35
MnO_2@CNTs//MnO_2@CNTs	2 mM HTEMPO & 1 M Na_2SO_4	1.0	56	31.2	16 000	96% (10 000-cycles)	36
GF@MNT@MNF//AC	1 M Na_2SO_4	1.8	51.50	23.2	119.9	80% (5000-cycles)	37
MoO_2//MnO_2	1 M Na_2SO_4	2.2	58.6	39.4	5500	93.75% (3000-cycles)	38
MnO_2/rGO//AC	1 M Na_2SO_4	2.0	45.25	25.14	250	—	39
$MnO_2/TiN/CC//Fe_2O_3/TiN/CC$	1 M Na_2SO_4	2.0	102.8	71.19	499.79	82.36% (10 000-cycles)	This work

the solution resistance (R_s) values before and after cycling are 1.5 and 3.2 Ω, respectively. The diameter of the semicircle of the Nyquist plots increases with the cycle number. Before cycling, the end of the semicircle is about 1.5 Ω and after 10 000 cycles, it is 1.8 Ω. The supercapacitor device before cycling has the shortest arc radius and largest slope of the inclined line in the low frequency region implying lower impedance and higher ion mobility. After 10 000 cycles, the electrical conductivity decreases somewhat because MnO_2 dissolves continuously and so the solution impedance increases with the cycle number.

The energy and power densities of MnO_2/TiN/CC//Fe_2O_3/TiN/CC as the device are calculated according to eqn (S2) and (S3)† and shown in Fig. 8(i). Similar Mn-based supercapacitors reported recently in the literature are compared in Fig. 8(i) and Table 1. The total mass of the active materials of MnO_2 is about 1 mg and the discharging time is considered in calculating the energy and power densities. The device shows a maximum energy density of 71.19 W h kg^{-1} at a power density of 499.79 W kg^{-1} and even at 5999.99 W kg^{-1}, it still shows an energy density of 31.3 W h kg^{-1}. As aforementioned above, this is one of the best values observed from similar devices regardless of the positive or negative configurations. For instance, it is better than those of K–MnO_2//AC (56 W h kg^{-1} at 550 W kg^{-1}),[32] M–MnO_2/rGO//AC (36.4 W h kg^{-1} at 212.5 W kg^{-1}),[33] rMnCo$_2$-O$_4$@rMnO$_2$-2 h//AC (32.4 W h kg^{-1} at 904.9 W kg^{-1}),[36] MnO_2@CNTs//MnO_2@CNTs (31.2 W h kg^{-1} at 16 000 W kg^{-1}),[34] and GF@MNT@MNF//AC (23.2 W h kg^{-1} at 119.9 W kg^{-1}).[36] The excellent electrochemical characteristics of the MnO_2/TiN/CC electrode and assembled supercapacitor device can be attributed to the shore-shell structure comprising the MnO_2 nanosheets and TiN nanowires that spread evenly on the conductive carbon cloth. In this way, the ion transport efficiency between the nanomaterials and electrolytes is improved while agglomeration of the nanomaterials can be mitigated. The Fe_2O_3/TiN/CC negative electrode shows good adaptability with the MnO_2-based positive electrode giving rise to enhanced cycling ability as well as large energy and power densities. As shown in the inset in Fig. 8(i), the flexible device maintains the good electrochemical activity even when it is bent mechanically.

5. Conclusion

Nanoscale MnO_2 and Fe_2O_3 are fabricated on TiN nanowires on a piece of conductive carbon cloth to form flexible electrodes for supercapacitors. The specific capacitances of MnO_2@TiN/CC at a current density of 3 mA cm^{-2} before and after 10 000 cycles are 310.7 F g^{-1} and 304.2 F g^{-1}, respectively, indicating a small loss of only 2.1%. An asymmetrical hybrid supercapacitor with MnO_2/TiN/CC as the positive electrode and Fe_2O_3/TiN/CC as the negative electrode is assembled. The device can withstand a high scanning rate of 5000 mV s^{-1} in the 2 V window. It shows a maximum energy density of 71.19 W h kg^{-1} at a power density of 499.79 W kg^{-1}, and even at 5999.99 W kg^{-1}, the energy density is still 31.3 W h kg^{-1}. The electrochemical results reveal that the MnO_2/TiN/CC and Fe_2O_3/TiN/CC electrodes have large potential in energy storage devices.

Conflicts of interest

There are no conflicts to declare.

Acknowledgements

References

1 Z. Ma, G. Shao, Y. Fan, G. Wang, J. Song and D. Shen, *ACS Appl. Mater. Interfaces*, 2016, **8**, 9050–9058.

2 X. Lang, A. Hirata, T. Fujita and M. Chen, *Nat. Nanotechnol.*, 2011, **6**, 232–236.

3 T. Li, J. Wu, X. Xiao, B. Zhang, Z. Hu, J. Zhou, P. Yang, X. Chen, B. Wang and L. Huang, *RSC Adv.*, 2016, **6**, 13914–13919.

4 L. F. Chen, Z. H. Huang, H. W. Liang, Q. F. Guan and S. H. Yu, *Adv. Mater.*, 2013, **25**, 4746.

5 H. Chen, L. Yu, J. M. Zhang and C. P. Liu, *Ceram. Int.*, 2016, 18058–18063.

6 A. Sumboja, C. Y. Foo, X. Wang and P. S. Lee, *Adv. Mater.*, 2013, **25**, 2809–2815.

7 F. Li, H. Chen, X. Y. Liu, S. J. Zhu, J. Q. Jia, C. H. Xu, F. Dong, Z. Q. Wen and Y. X. Zhang, *J. Mater. Chem. A*, 2016, **4**, 2096–2104.

8 J.-M. Jeong, S. H. Park, H. J. Park, S. B. Jin, S. G. Son, J.-M. Moon, H. Suh and B. G. Choi, *Adv. Funct. Mater.*, 2021, **31**, 2009632.

9 L. Bao, J. Zang and X. Li, *Nano Lett.*, 2011, **11**, 1215–1220.

10 K. Chanda, S. Maiti, S. Sarkar, P. Bairi, S. Thakur, K. Sardar, N. Besra, N. S. Das and K. K. Chattopadhyay, *ACS Appl. Nano Mater.*, 2021, **4**, 1420–1433.

11 Y. Zhu, H. Xu, J. Tang, X. Jiang, Y. Bao and Y. Chen, *J. Electrochem. Soc.*, 2021, **168**, 030542.

12 R. Liu, J. Duay and S. B. Lee, *ACS Nano*, 2011, **5**, 5608–5619.

13 S. Li, R. C. Feng, M. Li, X. Zhao, B. H. Zhang, Y. Liang, H. P. Ning, J. L. Wang, C. R. Wang and P. K. Chu, *RSC Adv.*, 2020, **10**, 37489.

14 R. R. Atram, V. M. Bhuse, R. G. Atram, C. M. Wu, P. Koinkar and S. B. Kondawar, *Mater. Chem. Phys.*, 2021, **262**, 124253.

15 R. Feng, M. Li, Y. Wang, J. Lin and P. K. Chu, *Electrochim. Acta*, 2021, 137716.

16 W. Diao, J. He, Q. Wang, X. Rao and Y. Zhang, *Catal. Sci. Technol.*, 2021, **11**, 230–238.

17 C. Chen and X. Yang, *RSC Adv.*, 2017, **7**, 56440–56446.

18 C. Wu, Y. N. Xu, L. Y. Ao, K. Jiang, L. Y. Shang, Y. W. Li, Z. G. Hu and J. H. Chu, *J. Alloys Compd.*, 2020, **816**(5), 152627.

19 Y. Zhang, Q. Li, J. Liu, W. You, F. Fang, M. Wang and R. Che, *Langmuir*, 2018, **34**, 5225–5233.

20 Y. Q. Lai, J. Li, H. S. Song, Z. A. Zhang, J. Li and Y. X. Liu, *J. Cent. South Univ. Technol.*, 2007, **5**, 633–637.

21 C. Wu, X. Y. Wang, B. W. Ju, Y. S. Bai, L. L. Jiang, H. Wu, Q. L. Zhao, J. Gao, X. Y. Wang and L. H. Yi, *J. Solid State Electrochem.*, 2013, **17**, 1693–1700.

22 W. Quan, C. H. Jiang, S. T. Wang, Y. S. Li, Z. T. Zhang, Z. L. Tang and F. Favier, *Electrochim. Acta*, 2017, **247**, 1072–01079.

23 B. Saravanakumar, S. S. Jayaseelan, M. K. Seo, H. Y. Kim and B. S. Kim, *Nanoscale*, 2017, **9**, 18819.

24 X. Wang, Y. P. He, Z. C. Guo, H. Huang, P. P. Zhang and H. B. Lin, *New J. Chem.*, 2019, **43**, 18813.

25 J. Wang, J. Polleux, J. Lim and B. Dunn, *J. Phys. Chem. A*, 2007, **111**, 14925–14931.

26 P. L. Taberna, P. Simon and J. F. Fauvarque, *J. Electrochem. Soc.*, 2003, **148**, A292.

27 J. M. Soon and K. P. Lo, *Electrochem. Solid-State Lett.*, 2007, **10**, A250–A254.

28 P. L. Taberna, P. Simon and J. F. Fauvarque, *J. Electrochem. Soc.*, 2003, **150**, A292–A300.

29 P. Sennu, V. Aravindan and Y.-S. Lee, *J. Power Sources*, 2016, **306**, 248–257.

30 B. Rfa, L. A. Mai, W. A. Yu, L. A. Jian, A. Kz, A. Jw, A. Cw and C. Pkc, *Electrochim. Acta*, 2021, **370**, 137716.

31 Y. Wang, X. Zhang, C. Guo, Y. Zhao, C. Xu, H. Li, Y. Wang, X. Zhang, C. Guo and Y. Zhao, *J. Mater. Chem. A*, 2013, **1**, 13290–13300.

32 N. Zarshad, A. U. Rahman, J. Wu, A. Ali, F. Raziq, L. Han, P. Wang, G. Li and H. Ni, *Chem. Eng. J.*, 2021, **415**, 128967.

33 L. Chen, H. Yin, Y. Zhang and H. Xie, *Nano*, 2020, **8**, 2050099.

34 Y. Zhang, Y. Liu, Z. Sun, Y. Bai, S. Cheng, P. Cui, J. Zhang, Q. Su, J. Fu and E. Xie, *Electrochim. Acta*, 2021, **375**, 137979.

35 M. He, L. L. Cao, W. L. Li, X. W. Chang and Z. Y. Ren, *J. Alloys Compd.*, 2021, **865**, 158934.

36 H. Liu, Z. Guo, S. Wang, X. Xun and J. Lian, *J. Alloys Compd.*, 2020, **846**, 156504.

37 R. Boopathiraja and M. Parthibavarman, *J. Alloys Compd.*, 2016, **811**, 152084.

38 C. Zhao, Y. Hu, Y. Zhou, N. Li, Y. Ding, J. Guo, C. Zhao and Y. Yang, *Energy Fuels*, 2021, **35**, 6909–6920.

39 S. Jangu, B. K. Satpathy, M. Raju, C. Jacob and D. Pradhan, *Dalton Trans.*, 2021, **50**, 6878–6888.